

On the electromagnetic-electron rings originating from the interaction of high-power short-pulse laser and underdense plasma

F SCI

Cite as: Phys. Plasmas **28**, 122104 (2021); <https://doi.org/10.1063/5.0065167>

Submitted: 30 July 2021 • Accepted: 07 November 2021 • Published Online: 06 December 2021

 P. Valenta,  G. M. Grittani,  C. M. Lazzarini, et al.

COLLECTIONS

 This paper was selected as Featured

 This paper was selected as Scilight



[View Online](#)



[Export Citation](#)



[CrossMark](#)

Physics of Plasmas
Papers from 62nd Annual Meeting of the
APS Division of Plasma Physics

Read now!

On the electromagnetic-electron rings originating from the interaction of high-power short-pulse laser and underdense plasma



Cite as: Phys. Plasmas **28**, 122104 (2021); doi: [10.1063/5.0065167](https://doi.org/10.1063/5.0065167)

Submitted: 30 July 2021 · Accepted: 7 November 2021 ·

Published Online: 6 December 2021



View Online



Export Citation



CrossMark

P. Valenta,^{1,2,a)} G. M. Grittani,¹ C. M. Lazzarini,^{1,2} O. Klimo,^{1,2} and S. V. Bulanov^{1,3}

AFFILIATIONS

¹ELI Beamlines Centre, Institute of Physics, Czech Academy of Sciences, Za Radnicí 835, 25241 Dolní Břežany Czech Republic

²Faculty of Nuclear Sciences and Physical Engineering, Czech Technical University in Prague, Břehová 7, 11519 Prague, Czech Republic

³Kansai Photon Science Institute, National Institutes for Quantum Science and Technology, Umemidai 8-1-7, Kizugawa, 619-0215 Kyoto, Japan

^{a)}Author to whom correspondence should be addressed: petr.valenta@eli-beams.eu

ABSTRACT

We investigate the evolution of radial profile of a high-power short-pulse laser interacting with underdense plasma, and in particular, we concentrate on the transverse electromagnetic rings, which are formed due to the laser radiation defocusing induced by the excitation of Langmuir waves. We illustrate the physical processes involved in the formation of such structures analytically and use the three-dimensional numerical simulations to reveal the relationships among the electromagnetic ring properties and the parameters of laser and plasma. Within the studied parameter range, we find that up to $\approx 70\%$ of the total initial driver pulse energy can be carried off by the electromagnetic rings having the opening angles ≈ 45 –115 mrad. Furthermore, we show that the electromagnetic rings can become a source of high-energy ring-shaped electron beams.

Published under an exclusive license by AIP Publishing. <https://doi.org/10.1063/5.0065167>

I. INTRODUCTION

A high-power laser pulse propagation in underdense plasmas is relevant to a number of scientific challenges, such as laser-driven acceleration of charged particles,^{1–3} development of sources of hard electromagnetic (EM) radiation,^{4,5} and nuclear fusion within the framework of the fast ignition concept.⁶ For many of these applications, it is essential that the laser pulse propagates over extended distances and transmits its energy into plasma in a controlled way without incurring excessive losses. At high laser power, relativistic effects change the properties of the collective response of the plasma. This concerns the propagation as qualitatively new processes occur, including relativistic self-focusing,^{7,8} filamentation,^{9,10} and formation of solitons^{11–14} and vortices.^{15,16}

In this context, much of the attention has been focused on the evolution of the radial profile of the laser beam in a fully ionized plasma. It turned out that the process of self-focusing for high-power laser pulses may lead to the formation of the multifilament and, in particular, ring-shaped transverse structures as reported in numerous theoretical and experimental works.^{17–25} In this paper, we present a

systematic study focused on the formation of the EM rings in the regime of high-power, ultrashort laser pulses, where the longitudinal charge separation and the generation of Langmuir waves cannot be neglected. The physical processes involved in the formation of the EM rings are illustrated using an analytical model based on the geometric optics approximation and demonstrated by a three-dimensional (3D) particle-in-cell (PIC) simulation. The properties of the EM rings are revealed by a multi-parametric PIC study for various plasma densities, laser intensities, and laser spot sizes. Furthermore, we show that the EM rings can become a source of high-energy ring-shaped electron beams.

The EM and electron ring structures are of interest for a number of potential applications. The EM rings, in the form of Laguerre–Gaussian laser pulses, have been studied as drivers for the plasma acceleration of electrons, positrons, and ions.^{26–32} The hollow electron ring structures have been considered as drivers for the plasma acceleration of positrons,^{33,34} as a source of high-flux x rays,³⁵ and as compact collimators for proton bunches in radio frequency accelerators.³⁶

In addition to the applications mentioned above, the understanding of the physical processes that lead to the generation of the EM and electron ring structures is important due to the following reasons: (i) The EM rings may carry off a significant fraction of energy from the driver and, thus, limit the overall efficiency of applications based on the laser-plasma interaction; (ii) the electron beams accelerated in the wake of the EM rings may cause damage to surrounding equipment (e.g., capillaries used for the laser pulse guiding) and become a source of unwanted EM radiation; and (iii) the knowledge of the origin of the EM and electron rings could serve as a diagnostic for determining the regimes of the laser-plasma interaction.

The paper is structured as follows. In Sec. II, we employ an analytical model to illustrate the radial evolution of the EM wave in the interaction with a Langmuir wave. In Sec. III, we present the setup and results of the 3D PIC simulation where the formation of the EM-electron rings is demonstrated. We also include the results of multi-parametric PIC study and describe the relationships among the EM ring properties and the parameters of laser and plasma. Finally, the results of this work are summarized and discussed in conclusion.

II. ELECTROMAGNETIC WAVE REFRACTION IN THE INTERACTION WITH LANGMUIR WAVE

First, we describe the distribution of electrons within the Langmuir wave. We assume that the plasma is cold and the ions are immobile. The continuity equation for the electron density n_e in one spatial dimension x and time t is

$$\frac{\partial n_e}{\partial t} + \frac{\partial}{\partial x}(n_e v_e) = 0, \quad (1)$$

where v_e is the electron velocity. We solve Eq. (1) using the quasistatic approximation, i.e., we make a mathematical transformation to the $\xi = x - v_{ph}t$ and $\tau = t$ coordinates, where v_{ph} is the phase velocity of the Langmuir wave, and neglect the $\partial/\partial\tau$ derivatives. We get

$$\frac{1}{n_e} \frac{\partial n_e}{\partial \xi} = \frac{1}{v_{ph} - v_e} \frac{\partial v_e}{\partial \xi}. \quad (2)$$

The solution of Eq. (2) is

$$n_e(\xi) = \frac{n_0 \beta_{ph}}{\beta_{ph} - \beta_e(\xi)}, \quad (3)$$

where n_0 is the electron density of ambient plasma, $\beta_{ph} = v_{ph}/c$, $\beta_e = v_e/c$, and c denotes the velocity of light in vacuum. When the denominator of Eq. (3) tends to zero, i.e., when the electron velocity approaches the phase velocity of the Langmuir wave, the electron density becomes infinite. This phenomenon is called the wave breaking. In what follows, we assume the Langmuir wave in the limit well below the wave breaking.

We consider that the Langmuir wave is generated by a given EM wave packet characterized by normalized vector potential $a = eE/m_e\omega c$, where E and ω are, respectively, the electric field and the angular frequency of the wave packet and m_e and $-e$ stand for the mass and charge of the electron, respectively. The distribution of the normalized electron velocity in the Langmuir wave can be approximated as $\beta_e \approx a_0^2 \cos(k_p \xi)/2$, where a_0 is the EM wave strength parameter, i.e., the peak amplitude of a in vacuum, and k_p is the

plasma wavenumber. Thus, the electron density distribution in the Langmuir wave is

$$n_e(\xi) = \frac{n_0 \beta_{ph}}{\beta_{ph} - a_0^2 \cos(k_p \xi)/2}. \quad (4)$$

This result can be generalized to the transverse direction r . As theoretically foreseen in Ref. 37 and later observed in a number of simulations and experiments,^{38–42} the density peaks of the Langmuir wave driven by a Gaussian pulse have the characteristic “horseshoe” shape and monotonically diminish with an increase in distance from the longitudinal axis. To take this into account, we extend Eq. (4) as follows:

$$n_e(\xi, r) = \frac{n_0 \beta_{ph}}{\beta_{ph} - a_0^2 \exp(-r^2/L^2) \cos(k_p \xi - r^2/L^2)/2}, \quad (5)$$

where L is the characteristic transverse size of the driver. The density distribution given by Eq. (5) for $a_0 = 0.6$, $\beta_{ph} = 0.95$ and $L = \lambda_p/2$, where $\lambda_p = 2\pi/k_p$ stands for the plasma wavelength, is shown in Fig. 1.

Second, we investigate the propagation of the EM wave packet (it can be, e.g., a rear part of the driver pulse or a separate “witness” pulse trailing behind the driver) in the plasma modulated by the Langmuir wave. The intensity of this EM wave packet is assumed to be low so that the plasma density given by Eq. (5) is unaffected by its propagation. Provided further that the wave packet is sufficiently short and its wavelength is small compared to the size of the Langmuir wave structures with which it interacts, its propagation can be described in the geometric optics approximation by examining the trajectories of particles (“photons”), each having a coordinate (ξ, r) and momentum (k_x, k_r) . The Hamiltonian for the photon interaction with the Langmuir wave is

$$\Omega(\xi, r, k_x, k_r) = \sqrt{k_x^2 + k_r^2 + n_e(\xi, r)} - \beta_{ph} k_x. \quad (6)$$

Here, k_x and k_r are measured in the units of ω/c and $n_e(\xi, r)$ is normalized by the critical plasma density $n_c = \sqrt{m_e \omega^2 / 4\pi e^2}$.

The trajectories of photons in plasma can be obtained by solving the set of Hamilton equations,

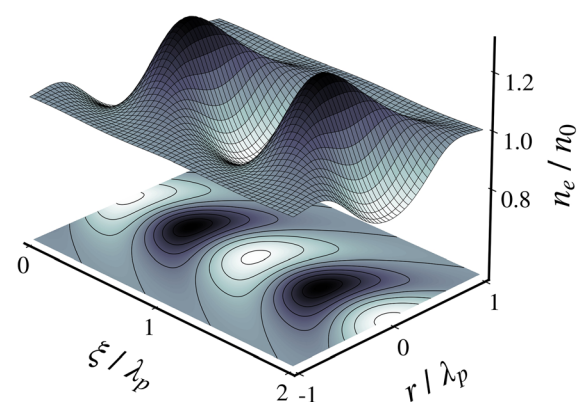


FIG. 1. Distribution of the normalized electron number density, n_e/n_0 , being perturbed by the action of the EM wave packet (i.e., the Langmuir wave) as described by Eq. (5) for $a_0 = 0.6$, $\beta_{ph} = 0.95$, and $L = \lambda_p/2$.

$$\begin{aligned} \frac{d\xi}{dt} &= \frac{k_x}{\sqrt{k_x^2 + k_r^2 + n_e(\xi, r)}} - \beta_{ph}, \\ \frac{dr}{d\xi} &= \frac{k_r}{k_x - \beta_{ph}\sqrt{k_x^2 + k_r^2 + n_e(\xi, r)}}, \\ \frac{dk_x}{d\xi} &= -\frac{1}{2} \frac{\partial n_e(\xi, r)}{\partial \xi} \frac{1}{k_x - \beta_{ph}\sqrt{k_x^2 + k_r^2 + n_e(\xi, r)}}, \\ \frac{dk_r}{d\xi} &= -\frac{1}{2} \frac{\partial n_e(\xi, r)}{\partial r} \frac{1}{k_x - \beta_{ph}\sqrt{k_x^2 + k_r^2 + n_e(\xi, r)}}. \end{aligned} \quad (7)$$

A numerical solution of the system of Eq. (7) for photons with several different initial values of r is displayed in Fig. 2. The photons initially propagate parallel to the Langmuir wave propagation direction with $k_x = 10$, whereas the Langmuir wave is described by Eq. (5) with $a_0 = 0.6$, $L = \lambda_p/2$, $n_0 = 0.01$, and $\beta_{ph} = 0.95$. The illustration shows that the trajectories of photons interacting with the Langmuir wave structures are curved toward and outward the propagation axis due to the changes in the plasma refractive index. In regions of electron density depressions (i.e., where $n_e/n_0 < 1$), the plasma enhances focusing. On the other hand, in regions of electron density peaks (i.e., where $n_e/n_0 > 1$), the plasma enhances defocusing. The focusing and defocusing of photons are, thus, induced by the excitation of the Langmuir wave. In addition, in the presence of plasma density gradients, the photons undergo energy (and, thus, the frequency) changes.^{43,44}

Since the plasma density profile and the initial photon distribution in Fig. 2 are axially symmetric, the defocused photons form a halo, which may in the high intensity limit evolve into an EM ring well separated from the axial part of the pulse (as shown in Sec. III). Provided that the EM ring contains a sufficient number of photons, it generates a secondary wakefield whose accelerating regions have

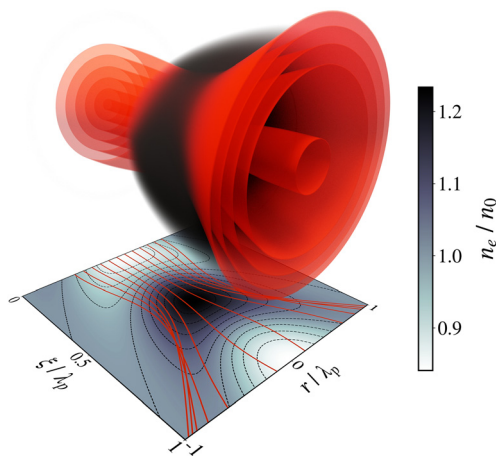


FIG. 2. Numerical solution of system of Eq. (7) showing the changes in the distribution of photons (reds) during their interaction with the Langmuir wave (grays). The photons, having several different initial values of r , initially propagate parallel to the Langmuir wave propagation direction (from left to right) with $k_x = 10$. The Langmuir wave is described by the parameters $a_0 = 0.6$, $L = \lambda_p/2$, $n_0 = 0.01$, and $\beta_{ph} = 0.95$. The projection at the bottom shows the photon trajectories (solid lines) and the normalized electron number density, n_e/n_0 , with its isocountours (grays and dashed lines) in the (ξ, r) -plane.

toroidal shapes (similar to those driven by Laguerre-Gaussian pulses^{26,27}). The electrons accelerated in such a wakefield may subsequently form ring-shaped structures as well. Since the properties of the EM and electron rings depend on the parameters of the generated Langmuir wave, they can be controlled by tuning the parameters of the driver and plasma.

A somewhat more rigorous analysis on how the transverse non-uniformities affect the evolution of an EM wave as it interacts with a Langmuir wave can be found in Ref. 37, where the authors consider predominantly the induced focusing. Here, we follow up on this work by studying the process of induced defocusing. We employ a model based on the approximation of geometric optics, which qualitatively illustrates the origin and the initial stage of the higher order Gaussian modes formation. Further evolution of the EM wave, which has to be treated self-consistently, particularly in the nonlinear case, is addressed by the 3D PIC simulations in the following section.

III. PARTICLE-IN-CELL SIMULATIONS

A. Simulation setup

In order to study the EM-electron ring formation self-consistently, we carry out a PIC simulation in the 3D Cartesian geometry using the fully relativistic EPOCH⁴⁵ code. The driver laser pulse is characterized by the strength parameter $a_0 = 16$ and by the angular frequency $\omega_0 = 2\pi c/\lambda_0$, where λ_0 is its wavelength in vacuum. The driver has Gaussian temporal and spatial profiles with the full-with-at-half-maximum duration $\tau_0 = 12 T_0$, where $T_0 = \lambda_0/c$ is the cycle period of the driver, and the beam waist (a radius at $1/e^2$ of the peak intensity) $w_0 = 6 \lambda_0$. The driver pulse, being linearly polarized along the z -axis, enters the simulation box from the left boundary and propagates parallel to the x -axis. Its focal spot is located at the distance of $500 \lambda_0$ from the boundary along the propagation direction. The corresponding energy, peak power, and peak intensity of the driver are, respectively, $\mathcal{E}_0 \approx 6 J \times \lambda_0 (\mu m)$, $P_0 \approx 200 \text{ TW}$, and $I_0 \approx 3.5 \times 10^{20} \text{ W/cm}^2 \times [\lambda_0 (\mu m)]^{-2}$. The peak driver electric field amplitude in vacuum is $E_0 = m_e c \omega_0 a_0 / e \approx 0.5 \text{ TV/cm} \times [\lambda_0 (\mu m)]^{-1}$.

The driver pulse propagates in a pre-ionized homogeneous hydrogen plasma with the electron number density $n_e = 5 \times 10^{-3} n_c$. The critical power for self-focusing⁷ is, thus, $P_c \approx 17.4 \text{ GW} \times n_c/n_e \approx 3.5 \text{ TW}$. (The pulse peak power exceeds this value by a factor of ≈ 57 .) The threshold for the Langmuir wave breaking⁴⁶ (and equally the threshold for the electron self-injection) is $E_{wb} = E_p \sqrt{2(\gamma_w - 1)} \approx 11.6 \text{ GV/cm} \times [\lambda_0 (\mu m)]^{-1}$, where $E_p = m_e \omega_p c / e$, $\gamma_w \approx \omega_0 / \omega_p$ is the relativistic factor of the Langmuir wave, and $\omega_p = \sqrt{4\pi n_e e^2 / m_e}$ is the Langmuir frequency. The plasma is cold and collisionless, and the electrons and protons are represented by quasi-particles with triangular shape functions. The initial number of quasi-particles per grid cell is 2 for both particle species.

The simulation utilizes the moving window technique. The simulation window, having the longitudinal and transverse dimensions of $80 \lambda_0$ and $150 \lambda_0$, respectively, moves along the driver propagation direction at a velocity equal to c . The underlying Cartesian grid is uniform with the resolution of 20 and 10 cells per λ_0 along the driver propagation direction and the transverse directions, respectively. The simulation is evolved over the time interval of $1200 T_0$. The equations of motion for quasi-particles are solved using the Boris algorithm,⁴⁷ and the EM fields are calculated using the standard second-order

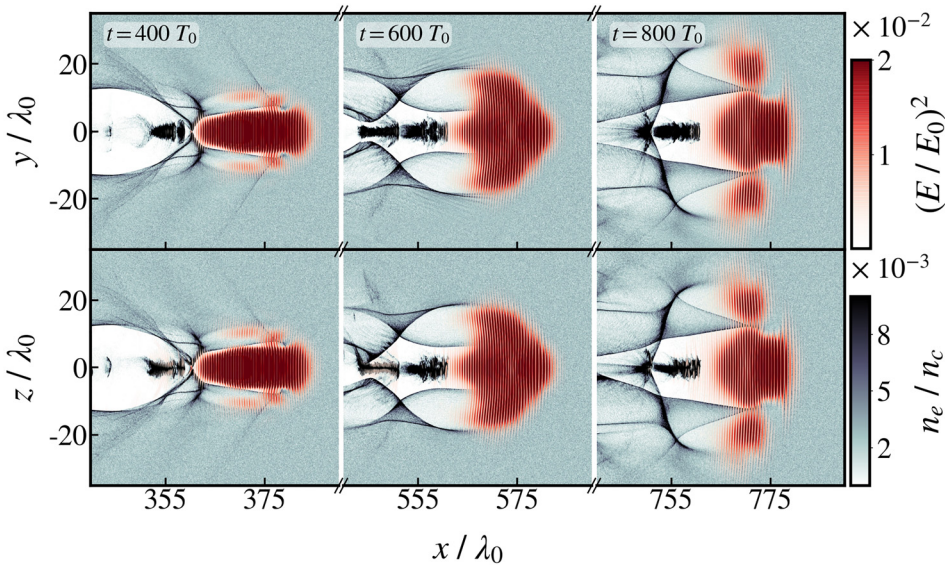


FIG. 3. Cross sections of the normalized driver field intensity, $(E/E_0)^2$, and the normalized electron number density, n_e/n_c , in the xy - and xz -planes at three successive instants of time obtained from the PIC simulation. The colorbars are saturated.

Yee solver⁴⁸ with the Courant -Friedrichs -Lowy (CFL) number⁴⁹ equal to 0.99. Absorbing boundary conditions are applied on each of the simulation domain sides for both the EM fields and particles.

B. Simulation results

The formation of the EM ring during the driver pulse propagation in plasma can be seen in Figs. 3 and 4. The relativistic self-focusing of the driver occurs as soon as it enters the plasma. Resulting tightly focused pulse ($t = 400 T_0$) reaches the peak amplitude of the normalized vector potential $a \approx 24.47$ (being $\approx 1.5 \times$ higher than a_0)

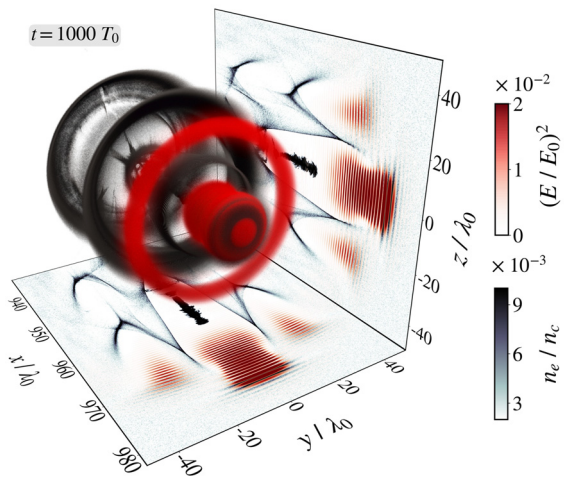


FIG. 4. 3D representation of the normalized driver field intensity, $(E/E_0)^2$, and the normalized electron number density, n_e/n_c , at the time $t = 1000 T_0$ obtained from the PIC simulation. Projections show the cross sections of the driver field intensity and the electron density in the xy - and xz -planes. The colorbars are saturated.

and pushes the plasma electrons not only along the laser axis, but also aside, creating a cavity void of electrons. At the same time, one may observe longitudinal wave breaking triggering the self-injection of electrons, part of which is being accelerated by the wakefield.

The cavity of the first Langmuir wave bucket is surrounded by a high-density electron sheath whose transverse size is smaller than the transverse size of the driver. Because of the strongly varying refractive index, a portion of the driver interacting with the inner surface of the cavity walls is focused toward the propagation axis forming a narrow density channel, which further guides the pulse. On the other hand, a portion of the driver interacting with the outer surface is pushed outward. This leads to a breakup of the driver into two distinct pulses ($t = 600 T_0$) according to the model presented in Sec. II. At $t = 800 T_0$, one can see that a ring of increased intensity encircling the axial part of the pulse is fully developed, whereas both parts are separated by a clear gap. A 3D representation of the driver field intensity and the electron density at $t = 1000 T_0$ is depicted in Fig. 4, where the EM ring is well visible.

Apart from the process of light defocusing induced by the plasma density variations described in Sec. II, the self-modulation instability (see, e.g., Refs. 50–52) may also contribute to the radial redistribution of the driver pulse energy. Its growth rate and other properties described in the literature may be applicable here as well. The self-modulation instability is closely related to Raman forward scattering, whose growth rate is⁵³

$$\Gamma_{\text{RFS}} = \frac{\omega_p^2 a_0}{\sqrt{8} \omega_0 (1 + a_0^2/2)}. \quad (8)$$

For the parameters of the simulation, the characteristic time $t_{\text{RFS}} = 1/\Gamma_{\text{RFS}} \approx 726 T_0$ is comparable to the timescale of the ring development seen in the simulation.

Figure 5 shows the time evolution of the areal energy density of the EM field,

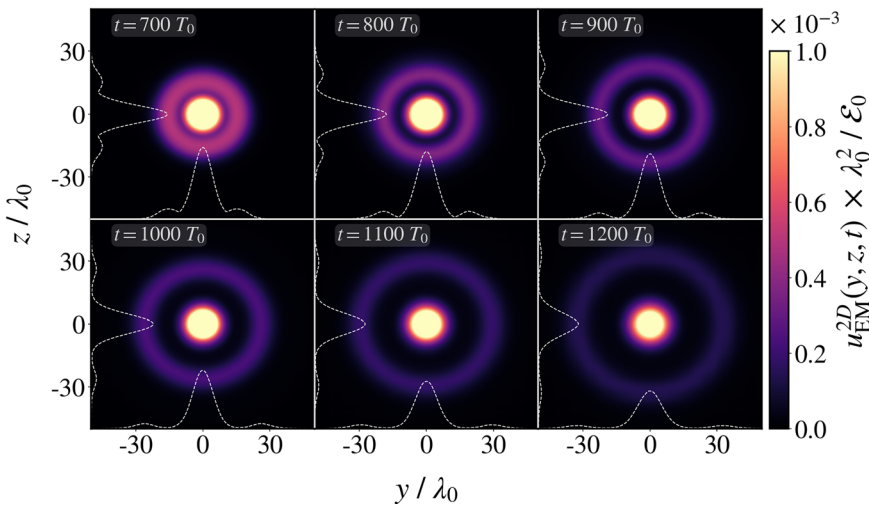


FIG. 5. The normalized areal energy density of the EM field, $u_{\text{EM}}^{2D}(y, z, t) \times \lambda_0^2 / \mathcal{E}_0$, defined by Eq. (9) at six successive instants of time obtained from the PIC simulation. The white dashed lines show the line-outs of the EM field areal energy density along the y - and z -axes. The colorbar is saturated.

$$u_{\text{EM}}^{2D}(y, z, t) = \int_{-\infty}^{+\infty} u_{\text{EM}}(x, y, z, t) dx. \quad (9)$$

Here, $u_{\text{EM}} = (E^2 + B^2)/8\pi$ is the EM field energy density, where E and B are, respectively, the electric and magnetic fields of the driver pulse. As can be seen, the EM ring is azimuthally symmetric with no observable nonuniformities in the energy distribution. While the ring expands radially outward, the energy of the axial part of the driver pulse is well confined within a density channel formed along the propagation axis. The radius of the density channel at the end of the simulation ($t = 1200 T_0$) is $R \approx 16 \lambda_0$.

For the purposes of more quantitative analysis of the EM ring, we define the following variable:

$$u_{\text{EM}}^{1D}(r, t) = \oint_l u_{\text{EM}}^{2D}(y, z, t) dl, \quad (10)$$

where l is the circle of radius r in the yz -plane, i.e., $y^2 + z^2 = r^2$. The time evolution of u_{EM}^{1D} is displayed in Fig. 6. As can be seen, this quantity develops two peaks: the first one (closer to the origin) corresponds to the axial part of the pulse and the second one (farther from the origin) corresponds to the EM ring. We denote $r_0(t)$ as a radial coordinate of minimum between the two peaks and $r_1(t)$ as a radial coordinate of maximum of the second peak (see Fig. 6).

Using the quantities described above, we define the instantaneous total EM ring energy,

$$\mathcal{E}_r(t) = \int_{r_0(t)}^{+\infty} u_{\text{EM}}^{1D}(r, t) dr, \quad (11)$$

and the instantaneous EM ring opening angle,

$$\theta_r(t) = 2 \arcsin \left(\frac{1}{v_g(t)} \frac{dr_1(t)}{dt} \right), \quad (12)$$

where $v_g(t)$ is the group velocity of the driver pulse. The time dependence of the quantities defined by Eqs. (11) and (12) is relatively weak within the timescale of the simulation; thus, in what follows, we consider the total EM ring energy, \mathcal{E}_r , and the EM ring opening angle, θ_r ,

to be the time-averaged values of $\mathcal{E}_r(t)$ and $\theta_r(t)$, respectively. Using these definitions, we find that $\mathcal{E}_r \approx 3.36 \text{ J} \times \lambda_0 (\mu\text{m})$ (which accounts for 56% of the initial total driver pulse energy) and $\theta_r \approx 68 \text{ mrad}$.

The accelerating regions of the wakefield left behind the EM ring are of toroidal shapes. The peak normalized vector potential of the EM ring decreases in time; it reaches $a \approx 3.97$ at the moment of detachment of the EM ring from the axial part of the driver ($t = 650 T_0$) and drops to $a \approx 1.74$ at the end of the simulation ($t = 1200 T_0$) mostly due to the EM ring radial expansion. The peak amplitude of the wakefield generated by the EM ring is less than E_{wb} and, thus, the self-injection of electrons does not occur. Figure 7 shows the time evolution of the areal kinetic energy density of electrons,

$$u_e^{2D}(y, z, t) = \int_{-\infty}^{+\infty} u_e(x, y, z, t) dx. \quad (13)$$

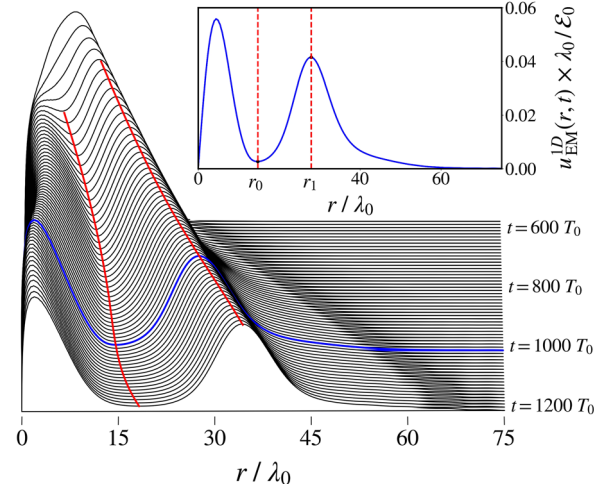


FIG. 6. The time evolution of $u_{\text{EM}}^{1D}(r, t) \times \lambda_0^2 / \mathcal{E}_0$ defined by Eq. (10) obtained from the PIC simulation. The inset shows $u_{\text{EM}}^{1D}(r, t) \times \lambda_0^2 / \mathcal{E}_0$ at $t = 1000 T_0$. The red lines mark r_0 and r_1 as defined in text.

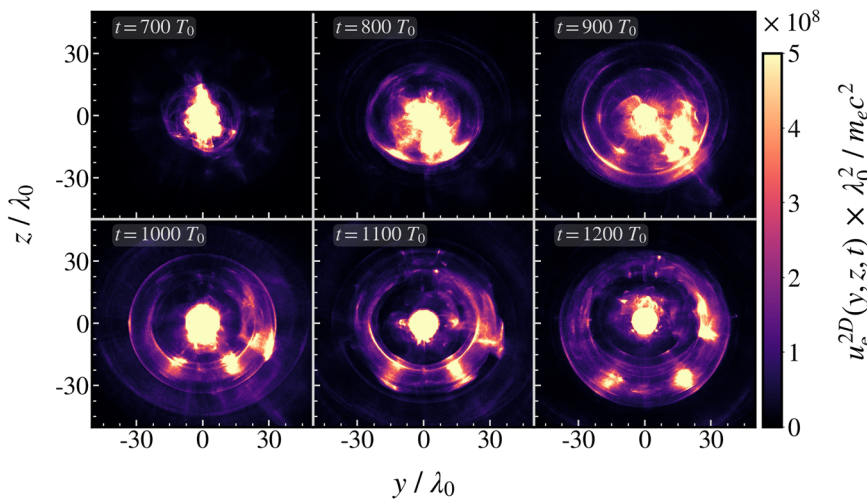


FIG. 7. The normalized areal kinetic energy density of electrons, $u_e^{2D}(y, z, t) \times \lambda_0^2 / m_e c^2$, defined by Eq. (13) at six successive instants of time obtained from the PIC simulation. The colorbar is saturated.

Here, u_e is the density of the electron kinetic energy $\mathcal{E}_e = m_e c^2 (\gamma_e - 1)$, where γ_e is the relativistic factor of electrons. Although the EM ring does not trigger the self-injection, we may observe an increased electron energy density along a ring encircling the axial electron beam; it consists of a lower energy density ring segments and unevenly distributed spots of local energy density enhancements. Resulting ring-shaped electron beam inherits the opening angle from the EM ring.

The spots of higher electron energy density emerge in certain prominent directions with respect to the driver propagation axis. In order to unveil the origin of their formation, in Fig. 8, we plot the cross sections of the electron energy density together with the electron number density and the longitudinal electric field in the xh -plane, where h is a line in the yz -plane along which one of the spots appears. As the figure indicates, the spots of higher energy density are formed by the

electrons injected into the second period of the Langmuir wave. They exhibit a spiral motion ($t = 600 T_0$) due to the focusing forces of the wakefield and a nonzero transverse momentum of electrons at the moment of injection. Later on ($t = 800 T_0$), a large fraction of these electrons is dragged into the secondary wakefield generated by the EM ring. The direction of the drag is determined by the instantaneous position of the electrons on the spiral at the moment of the EM ring detachment from the axial part of the pulse.

On the other hand, the lower energy density ring segments are formed by the electrons injected into the first period of the Langmuir wave. When the EM ring detaches from the driver, the energy of the axial part of the pulse drops and the wake structure shrinks longitudinally ($t = 700 T_0$). The electrons from the rear part of the beam consequently find themselves in the defocusing and decelerating

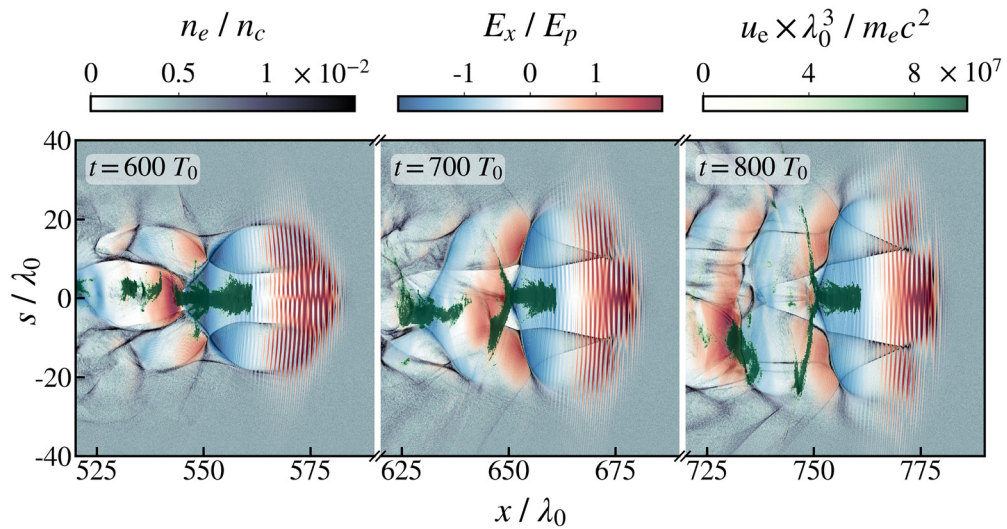


FIG. 8. Cross sections of the normalized electron number density, n_e / n_c , the normalized longitudinal electric field, E_x / E_p , and the normalized kinetic energy density of electrons, $u_e \times \lambda_0^3 / m_e c^2$, in the xh -plane at three successive instant of time obtained from the PIC simulation, where h is a line in the yz -plane defined using parameter s as $y = s \cos \varphi$, $z = s \sin \varphi$ with $\varphi = 2.27$ rad. The colorbars are saturated.

region of the wakefield. These electrons are then as well directed into the second period of the secondary wakefield generated by the EM ring. However, their distribution is much more azimuthally uniform.

The energy spectra of the electrons located in the region defined by $r \leq r_0(t)$ (i.e., the electrons in the vicinity of the driver propagation axis) and of the electrons located in the region defined by $r > r_0(t)$ (i.e., the electrons at the periphery) at the end of the simulation ($t = 1200 T_0$) are shown in Fig. 9. They reveal that the axial electron beam possesses a relatively broad energy peak at ≈ 130 MeV on the background of quasi-thermal spectrum. As far as the ring-shaped electron beam is concerned, one can distinguish peaks around ≈ 25 MeV and ≈ 50 MeV corresponding, respectively, to the populations of electrons forming the lower energy density ring segments and the higher energy density spots. The charge of electrons having the kinetic energy > 10 MeV in the vicinity of the driver propagation axis and at the periphery is, respectively, ≈ 4.36 nC and ≈ 1.68 nC. The ring electrons, thus, carry up to 28% of the total electron beam charge.

We emphasize that the purpose of the electron analysis above is solely to show that the EM ring can become a source of ring-shaped high-energy electron beams. In this work, no effort has been made in order to optimize the parameters of the electron beams for specific applications. Regarding the optimization and tuning of the electron beam parameters, the reader can refer to the theory of laser-wakefield acceleration.^{1,2} Furthermore, we note that the emissions of the electron ring patterns from the laser-plasma interaction have been also reported in other works and several different mechanisms of their origin have been identified (see, e.g., Refs. 35 and 54–60).

C. Multi-parametric study

In order to find out whether the properties of the generated EM rings are sensitive to changes in the parameters of laser and plasma and, if so, to explain the relationships among them, we carry out a multi-parametric PIC study. We perform numerous 3D PIC simulations where we vary the values of the ambient plasma electron density, n_0 , the laser strength parameter, a_0 , and the laser beam waist, w_0 . All other simulation parameters remain the same as for the simulation described in Sec. III A except for the Cartesian grid resolution and the number of quasi-particles per grid cell. In order to reduce the

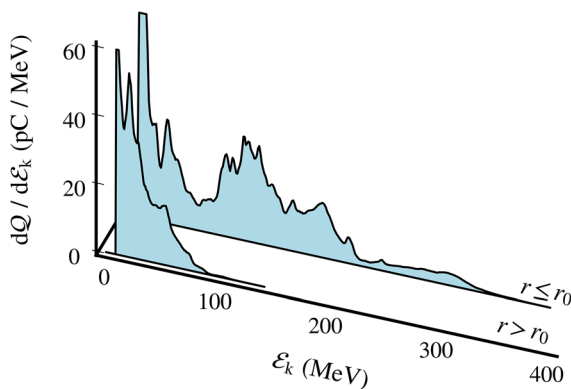


FIG. 9. Energy spectra of the electrons located in the region defined by $r \leq r_0(t)$ and in the region defined by $r > r_0(t)$ at the end of the PIC simulation ($t = 1200 T_0$).

computational demands of the simulations, the grid resolution is twice as low and the number of quasi-particles per grid cell for both particle species is set to 1. We ensured, however, that such a simulation setup is justified by performing several simulations with higher resolution and number of quasi-particles that resulted in negligible differences in the properties of interest of the EM rings.

First, we compare the results of simulations where solely the laser strength parameter is varied. Figure 10 shows the quantity u_{EM}^{1D} defined by Eq. (10) for a_0 ranging from 4 to 20. It can be clearly seen that the portion of the energy leakage from the laser pulse increases with a_0 until it saturates at certain value. While for $a_0 \geq 6$, the leaked part of the pulse forms a distinct EM ring separated from the axial pulse by a clear gap, for $a_0 < 6$, we observe rather a broad low intensity halo instead of the EM ring, which is in accordance with the analytical model introduced in Sec. II. The onset of the EM ring formation occurs when the power of the leaked part of the pulse exceeds the critical power for self-guiding in plasma. In the studied case, this corresponds to a_0 somewhere between 4 and 6 (or to P_0/P_c in the range from 3.5 to 8). For $a_0 \leq 2$, the self-focusing of the laser pulse does not happen, and, consequently, the energy leakage is negligible. For this reason, we do not include the results here.

The dependence of the ratio of the total EM ring energy to the total initial driver pulse energy and the EM ring opening angle on the laser strength parameter is shown in Fig. 11. We note that since for $a_0 < 6$ the EM rings do not occur, we cannot include their attributes in this comparison. Figure 11 reveals that the portion of energy in the EM ring grows with a_0 until it saturates at $\approx 57\%$ of \mathcal{E}_0 for $a_0 \geq 16$. This growth can be explained by the fact that stronger driver yields steeper electron density gradients, which then defocus the interacting parts of the pulse more effectively. On the contrary, the opening angle decreases with a_0 , from ≈ 100 mrad for $a_0 = 6$ to ≈ 63 mrad for $a_0 = 20$. As one can see from Fig. 12, the opening angle of the EM ring correlates with the elongation of the ion cavity and the surrounding electron wall. The larger the elongation of the cavity, the smaller the opening angle of the EM ring.

Second, we compare the results of simulations where the laser strength parameter is varied alongside the laser beam waist and the electron density. Figure 13 shows the dependence of $\mathcal{E}_r/\mathcal{E}_0$ and θ_r on n_0 , a_0 , and w_0 , where a_0 is varied from 14 to 18, n_0 is varied from

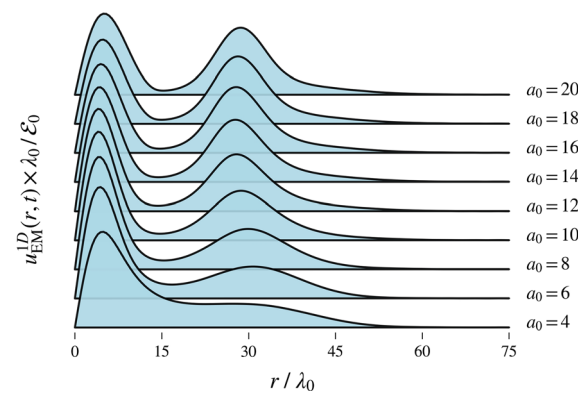


FIG. 10. The quantity $u_{\text{EM}}^{1D}(r, t) \times \lambda_0^2 / \mathcal{E}_0$ defined by Eq. (10) for several different laser strength parameters, a_0 , at $t = 1000 T_0$ obtained from the PIC simulations.

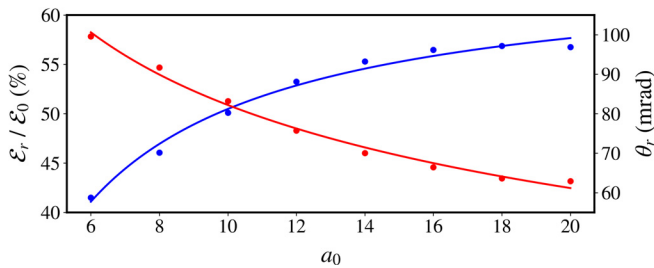


FIG. 11. The ratio of the total EM ring energy to the total initial driver pulse energy, $\mathcal{E}_r / \mathcal{E}_0$, (blue) and the EM ring opening angle, θ_r (red) for several different laser strength parameters, a_0 . The dots mark the values obtained from the PIC simulations, and the lines are curves fitting the data.

0.4 % of n_c to 0.6 % of n_c , and w_0 is varied from $4\lambda_0$ to $8\lambda_0$. Within the studied parameter range, we see that both $\mathcal{E}_r / \mathcal{E}_0$ and θ_r increase strongly with the decrease in the driver beam waist. The portions of energy carried off by the EM rings vary from ≈ 45 to ≈ 49 % of \mathcal{E}_0 for $w_0 = 8\lambda_0$, from ≈ 55 to ≈ 58 % of \mathcal{E}_0 for $w_0 = 6\lambda_0$, and from ≈ 65 to ≈ 68 % of \mathcal{E}_0 for $w_0 = 4\lambda_0$. The opening angles of the EM rings vary from ≈ 47 to ≈ 60 mrad for $w_0 = 8\lambda_0$, from ≈ 58 to ≈ 73 mrad for $w_0 = 6\lambda_0$, and from ≈ 85 to ≈ 115 mrad for $w_0 = 4\lambda_0$.

For a fixed driver beam waist, the dependence of $\mathcal{E}_r / \mathcal{E}_0$ and θ_r on the electron density and the laser strength parameter is more complex. In the case of $w_0 = 8\lambda_0$, we observe that the value of $\mathcal{E}_r / \mathcal{E}_0$ depends predominantly on the electron density, both quantities being inversely proportional to each other. On the contrary, when $w_0 = 4\lambda_0$, the value of $\mathcal{E}_r / \mathcal{E}_0$ depends mainly on a_0 and the proportionality is direct. As for the opening angle of the EM ring, it is inversely proportional to both a_0 and n_0 or, equivalently, inversely proportional to the ratio between the driver pulse peak power and the critical power for self-focusing, P_0 / P_c , regardless the value of w_0 . The relationships between the EM ring properties and the parameters of laser and plasma can be again explained (from the most part) by the dynamical evolution of the Langmuir wave, particularly the shape and steepness of its density peaks, excited by the driver pulse.

The results of the multi-parametric study reveal that the EM rings are present in a relatively broad range of studied cases (always

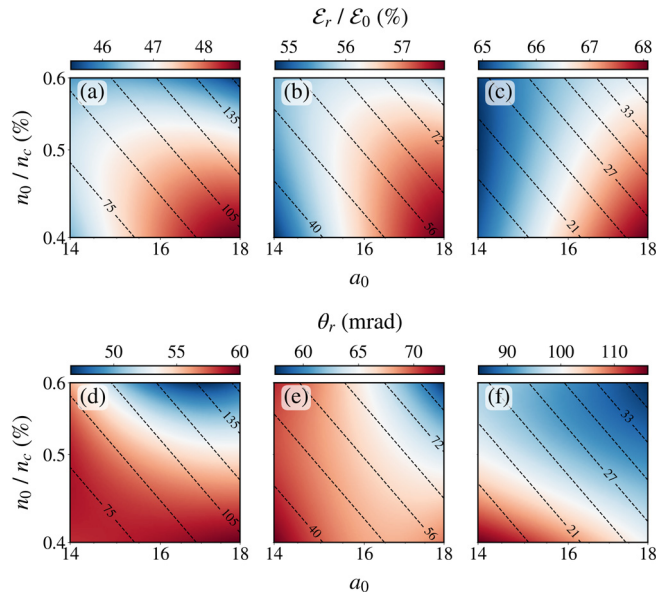


FIG. 13. The ratio of the total EM ring energy to the total initial driver pulse energy, $\mathcal{E}_r / \mathcal{E}_0$, dependence on the normalized ambient plasma electron density, n_0 / n_c , the laser strength parameter, a_0 , and the laser beam waist: (a) $w_0 = 8\lambda_0$, (b) $w_0 = 6\lambda_0$, and (c) $w_0 = 4\lambda_0$. The EM ring opening angle, θ_r , dependence on the normalized ambient plasma electron density, n_0 / n_c , the laser strength parameter, a_0 , and the laser beam waist: (d) $w_0 = 8\lambda_0$, (e) $w_0 = 6\lambda_0$, and (f) $w_0 = 4\lambda_0$. The scattered data obtained from the PIC simulations are interpolated using the radial basis function interpolation with Gaussian kernel and the shape parameter $\varepsilon = 10$. The black dashed lines are the isocontours of the ratio between the driver pulse peak power and the critical power for self-focusing, P_0 / P_c .

together with the axial part of the pulse). This fact indicates that the EM rings are rather robust nonlinear EM objects. Furthermore, all the EM rings exhibit surprisingly high azimuthal symmetry, with very weak sensitivity to the laser polarization. It is known, however, that the ring modes are unstable to azimuthal perturbations. Their stability against symmetric and asymmetric azimuthal perturbations have been investigated in detail in Ref. 23. Finally, this multi-parametric study

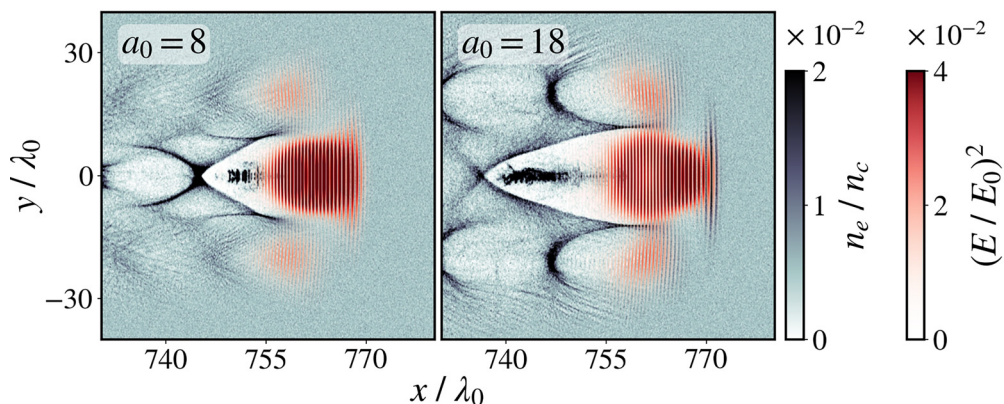


FIG. 12. Cross sections of the normalized driver field intensity, $(E/E_0)^2$, and the normalized electron density, n_e/n_c , in the xy -plane for $a_0 = 8$ ($\theta_r \approx 93.8$ mrad) and $a_0 = 18$ ($\theta_r \approx 66.1$ mrad) at $t = 800 T_0$ obtained from the PIC simulations. The colorbars are saturated.

verifies that the properties of the EM rings (and consequently the properties of the ring-shaped electron beams) can be controlled by tuning the parameters of the laser and plasma.

IV. CONCLUSION

In this paper, we investigate the interaction of Langmuir waves with driving laser pulses as they co-propagate in underdense plasma. We observe the formation of ring-shaped EM-electron structures, where the EM rings arise from the laser pulse defocusing induced by the excitation of Langmuir waves in underdense plasma, and the ring-shaped electron beams are formed and accelerated subsequently by the secondary toroidal wakefields generated by the EM rings. The underlying physical process of laser radiation defocusing by the electron density modulations in the Langmuir wave is illustrated using an analytical model based on the geometric optics approximation and demonstrated by a 3D PIC simulation. A multi-parametric PIC study further reveals that the EM rings are relatively robust nonlinear objects, whose properties can be controlled by tuning the parameters of laser and plasma. Within the studied parameter range, we find that up to $\approx 70\%$ of the total initial driver pulse energy can be carried off by the EM rings having the opening angles $\approx 45\text{--}115$ mrad.

The results obtained are important in the sense that the generated EM ring structures may carry off a significant fraction of energy from the driver and, thus, limit the overall efficiency of applications based on the laser-plasma interaction. Furthermore, the relatively wide-angle electron beams accelerated in the wake of the EM rings may cause a damage to surrounding equipment and become a source of unwanted EM radiation. Finally, the understanding of the EM-electron ring origins could serve as a diagnostics for determining the regimes of laser-plasma interaction and contribute to the development of numerous practical applications.^{26–36}

ACKNOWLEDGMENTS

This work was supported by the projects “High Field Initiative” (Grant No. CZ.02.1.01/0.0/0.0/15_003/0000449) from the European Regional Development Fund and “e-INFRA CZ” (ID:90140) from the Ministry of Education, Youth and Sports of the Czech Republic. The EPOCH code was in part funded by the UK EPSRC Grant Nos. EP/G054950/1, EP/G056803/1, EP/G055165/1, and EP/M022463/1.

AUTHOR DECLARATIONS

Conflict of Interest

The authors have no conflicts of interest to disclose.

DATA AVAILABILITY

The data that support the findings of this study are openly available in a Zenodo repository titled “On the electromagnetic-electron rings originating from the interaction of high-power short-pulse laser and underdense plasma” at <https://doi.org/10.5281/zenodo.5711101>.

REFERENCES

- ¹T. Tajima and J. M. Dawson, *Phys. Rev. Lett.* **43**, 267 (1979).
- ²E. Esarey, C. B. Schroeder, and W. P. Leemans, *Rev. Mod. Phys.* **81**, 1229 (2009).
- ³A. J. Gonsalves, K. Nakamura, J. Daniels, C. Benedetti, C. Pieronek, T. C. De Raadt, S. Steinke, J. H. Bin, S. S. Bulanov, J. Van Tilborg, C. G. Geddes, C. B. Schroeder, C. Tóth, E. Esarey, K. Swanson, L. Fan-Chiang, G. Bagdasarov, N. Bobrova, V. Gasilov, G. Korn, P. Sasorov, and W. P. Leemans, *Phys. Rev. Lett.* **122**, 084801 (2019).
- ⁴S. V. Bulanov, T. Z. Esirkepov, M. Kando, A. S. Pirozhkov, and N. N. Rosanov, *Phys.-Usp.* **56**, 429 (2013).
- ⁵A. S. Pirozhkov, M. Kando, T. Z. Esirkepov, P. Gallegos, H. Ahmed, E. N. Ragozin, A. Y. Faenov, T. A. Pikuz, T. Kawachi, A. Sagisaka, J. K. Koga, M. Courty, J. Green, P. Foster, C. Brenner, B. Dromey, D. R. Symes, M. Mori, K. Kawase, T. Kameshima, Y. Fukuda, L. Chen, I. Daito, K. Ogura, Y. Hayashi, H. Kotaki, H. Kiriyama, H. Okada, N. Nishimori, T. Imazono, K. Kondo, T. Kimura, T. Tajima, H. Daido, P. Rajeev, P. McKenna, M. Borghesi, D. Neely, Y. Kato, and S. V. Bulanov, *Phys. Rev. Lett.* **108**, 135004 (2012).
- ⁶M. Tabak, J. Hammer, M. E. Glinsky, W. L. Krueer, S. C. Wilks, J. Woodworth, E. M. Campbell, M. D. Perry, and R. J. Mason, *Phys. Plasmas* **1**, 1626 (1994).
- ⁷G.-Z. Sun, E. Ott, Y. C. Lee, and P. Guzdar, *Phys. Fluids* **30**, 526 (1987).
- ⁸P. Monot, T. Auguste, P. Gibbon, F. Jakober, G. Mainfray, A. Dulieu, M. Louis-Jacquet, G. Malka, and J. L. Miquel, *Phys. Rev. Lett.* **74**, 2953 (1995).
- ⁹P. E. Young and P. R. Bolton, *Phys. Rev. Lett.* **77**, 4556 (1996).
- ¹⁰N. M. Naumova, S. V. Bulanov, K. Nishihara, T. Z. Esirkepov, and F. Pegoraro, *Phys. Rev. E* **65**, 045402(R) (2002).
- ¹¹T. Z. Esirkepov, F. F. Kamenets, S. V. Bulanov, and N. M. Naumova, *JETP Lett.* **68**, 36 (1998).
- ¹²S. V. Bulanov, T. Z. Esirkepov, N. M. Naumova, and V. A. Vshivkov, *Phys. Rev. Lett.* **82**, 3440 (1999).
- ¹³D. Farina and S. V. Bulanov, *Phys. Rev. Lett.* **86**, 5289 (2001).
- ¹⁴T. Z. Esirkepov, K. Nishihara, S. V. Bulanov, and F. Pegoraro, *Phys. Rev. Lett.* **89**, 275002 (2002).
- ¹⁵S. V. Bulanov, M. Lontano, T. Z. Esirkepov, F. Pegoraro, and A. M. Pukhov, *Phys. Rev. Lett.* **76**, 3562 (1996).
- ¹⁶D. N. Yue, M. Chen, P. F. Geng, X. H. Yuan, S. M. Weng, S. S. Bulanov, S. V. Bulanov, K. Mima, Z. M. Sheng, and J. Zhang, *Phys. Plasmas* **28**, 042303 (2021).
- ¹⁷W. B. Mori, C. Joshi, J. M. Dawson, D. W. Forslund, and J. M. Kindel, *Phys. Rev. Lett.* **60**, 1298 (1988).
- ¹⁸B. I. Cohen, B. F. Lasinski, A. B. Langdon, and J. C. Cummings, *Phys. Fluids B* **3**, 766 (1991).
- ¹⁹A. B. Borisov, A. V. Borovskiy, O. B. Shiryaev, V. V. Korobkin, A. M. Prokhorov, J. C. Solem, T. S. Luk, K. Boyer, and C. K. Rhodes, *Phys. Rev. A* **45**, 5830 (1992).
- ²⁰K. Krushelnick, A. Ting, C. I. Moore, H. R. Burris, E. Esarey, P. Sprangle, and M. Baine, *Phys. Rev. Lett.* **78**, 4047 (1997).
- ²¹F. Cattani, A. Kim, D. Anderson, and M. Lisak, *Phys. Rev. E* **64**, 016412 (2001).
- ²²A. Kim, M. Tushentsov, F. Cattani, D. Anderson, and M. Lisak, *Phys. Rev. E* **65**, 036416 (2002).
- ²³N. Naseri, W. Rozmus, and D. Pesme, *Phys. Plasmas* **23**, 113101 (2016).
- ²⁴V. F. Kovalev and V. Y. Bychenkov, *Phys. Rev. E* **99**, 043201 (2019).
- ²⁵P. Valenta, G. M. Grittani, C. M. Lazzarini, O. Klimo, and S. V. Bulanov, in *Laser Acceleration of Electrons, Protons, and Ions VI*, edited by S. S. Bulanov, J. Schreiber, and C. B. Schroeder (International Society for Optics and Photonics, SPIE, 2021), Vol. 11779, p. 1177909.
- ²⁶P. Michel, E. Esarey, C. B. Schroeder, B. A. Shadwick, and W. P. Leemans, *Phys. Plasmas* **13**, 113112 (2006).
- ²⁷J. Vieira and J. T. Mendonça, *Phys. Rev. Lett.* **112**, 215001 (2014).
- ²⁸G. B. Zhang, M. Chen, C. B. Schroeder, J. Luo, M. Zeng, F. Y. Li, L. L. Yu, S. M. Weng, Y. Y. Ma, T. P. Yu, Z. M. Sheng, and E. Esarey, *Phys. Plasmas* **23**, 033114 (2016).
- ²⁹Z. Y. Xu, C. F. Xiao, H. Y. Lu, R. H. Hu, J. Q. Yu, Z. Gong, Y. R. Shou, J. X. Liu, C. Z. Xie, S. Y. Chen, H. G. Lu, T. Q. Xu, R. X. Li, N. Hafz, S. Li, Z. Najmudin, P. P. Rajeev, D. Neely, and X. Q. Yan, *Phys. Rev. Accel. Beams* **23**, 091301 (2020).
- ³⁰X. Zhang, B. Shen, L. Zhang, J. Xu, X. Wang, W. Wang, L. Yi, and Y. Shi, *New J. Phys.* **16**, 123051 (2014).
- ³¹C. Brabetz, S. Busold, T. Cowan, O. Deppert, D. Jahn, O. Kester, M. Roth, D. Schumacher, and V. Bagnoud, *Phys. Plasmas* **22**, 013105 (2015).
- ³²W. P. Wang, C. Jiang, H. Dong, X. M. Lu, J. F. Li, R. J. Xu, Y. J. Sun, L. H. Yu, Z. Guo, X. Y. Liang, Y. X. Leng, R. X. Li, and Z. Z. Xu, *Phys. Rev. Lett.* **125**, 034801 (2020).
- ³³N. Jain, T. M. Antonsen, and J. P. Palastro, *Phys. Rev. Lett.* **115**, 195001 (2015).

- ³⁴N. Jain, *Phys. Plasmas* **26**, 023107 (2019).
- ³⁵T. Z. Zhao, K. Behm, C. F. Dong, X. Davoine, S. Y. Kalmykov, V. Petrov, V. Chvykov, P. Cummings, B. Hou, A. Maksimchuk, J. A. Nees, V. Yanovsky, A. G. Thomas, and K. Krushelnick, *Phys. Rev. Lett.* **117**, 094801 (2016).
- ³⁶G. Stancari, A. Valishev, G. Annala, G. Kuznetsov, V. Shiltsev, D. A. Still, and L. G. Vorobiev, *Phys. Rev. Lett.* **107**, 084802 (2011).
- ³⁷S. V. Bulanov and A. S. Sakharov, *JETP Lett.* **54**, 203 (1991).
- ³⁸S. V. Bulanov, F. Pegoraro, and A. M. Pukhov, *Phys. Rev. Lett.* **74**, 710 (1995).
- ³⁹B. A. Shadwick, G. M. Tarkenton, E. H. Esarey, and W. P. Leemans, *IEEE Trans. Plasma Sci.* **30**, 38 (2002).
- ⁴⁰N. H. Matlis, S. Reed, S. S. Bulanov, V. Chvykov, G. Kalintchenko, T. Matsuoka, P. Rousseau, V. Yanovsky, A. Maksimchuk, S. Kalmykov, G. Shvets, and M. C. Downer, *Nat. Phys.* **2**, 749 (2006).
- ⁴¹A. Maksimchuk, S. Reed, S. S. Bulanov, V. Chvykov, G. Kalintchenko, T. Matsuoka, C. McGuffey, G. Mourou, N. Naumova, J. Nees, P. Rousseau, V. Yanovsky, K. Krushelnick, N. H. Matlis, S. Kalmykov, G. Shvets, M. C. Downer, C. R. Vane, J. R. Beene, D. Stracener, and D. R. Schultz, *Phys. Plasmas* **15**, 056703 (2008).
- ⁴²M. C. Downer, R. Zgadzaj, A. Debus, U. Schramm, and M. C. Kaluza, *Rev. Mod. Phys.* **90**, 035002 (2018).
- ⁴³S. C. Wilks, J. M. Dawson, W. B. Mori, T. Katsouleas, and M. E. Jones, *Phys. Rev. Lett.* **62**, 2600 (1989).
- ⁴⁴T. Z. Esirkepov, S. V. Bulanov, M. Yamagiwa, and T. Tajima, *Phys. Rev. Lett.* **96**, 014803 (2006).
- ⁴⁵T. D. Arber, K. Bennett, C. S. Brady, A. Lawrence-Douglas, M. G. Ramsay, N. J. Sircombe, P. Gillies, R. G. Evans, H. Schmitz, A. R. Bell, and C. P. Ridgers, *Plasma Phys. Controlled Fusion* **57**, 113001 (2015).
- ⁴⁶A. Akhiezer and R. Polovin, Sov. Phys. JETP **3**, 696 (1956).
- ⁴⁷J. P. Boris, in *Proceedings of the Fourth Conference on Numerical Simulation of Plasmas* (Office of Naval Research, Arlington, VA, 1971), pp. 3–67.
- ⁴⁸K. S. Yee, *IEEE Trans. Antennas Propag.* **14**, 302 (1966).
- ⁴⁹R. Courant, K. Friedrichs, and H. Lewy, *Math. Ann.* **100**, 32 (1928).
- ⁵⁰T. M. Antonsen and P. Mora, *Phys. Rev. Lett.* **69**, 2204 (1992).
- ⁵¹P. Sprangle, E. Esarey, J. Krall, and G. Joyce, *Phys. Rev. Lett.* **69**, 2200 (1992).
- ⁵²N. Andreev, L. Gorbunov, V. Kirsanov, A. Pogosova, R. Ramazashvili, and D. Parsons, *JETP Lett.* **55**, 571 (1992).
- ⁵³W. B. Mori, C. D. Decker, D. E. Hinkel, and T. Katsouleas, *Phys. Rev. Lett.* **72**, 1482 (1994).
- ⁵⁴D. Kaganovich, D. F. Gordon, and A. Ting, *Phys. Rev. Lett.* **100**, 215002 (2008).
- ⁵⁵L. Zhang, L. M. Chen, W. M. Wang, W. C. Yan, D. W. Yuan, J. Y. Mao, Z. H. Wang, C. Liu, Z. W. Shen, A. Faenov, T. Pikuz, D. Z. Li, Y. T. Li, Q. L. Dong, X. Lu, J. L. Ma, Z. Y. Wei, Z. M. Sheng, and J. Zhang, *Appl. Phys. Lett.* **100**, 014104 (2012).
- ⁵⁶B. B. Pollock, F. S. Tsung, F. Albert, J. L. Shaw, C. E. Clayton, A. Davidson, N. Lemos, K. A. Marsh, A. Pak, J. E. Ralph, W. B. Mori, and C. Joshi, *Phys. Rev. Lett.* **115**, 055004 (2015).
- ⁵⁷X. Yang, E. Brunetti, D. R. Gil, G. H. Welsh, F. Y. Li, S. Cipiccia, B. Ersfeld, D. W. Grant, P. A. Grant, M. R. Islam, M. P. Tooley, G. Vieux, S. M. Wiggins, Z. M. Sheng, and D. A. Jaroszynski, *Sci. Rep.* **7**, 43910 (2017).
- ⁵⁸E. Brunetti, X. Yang, F. Y. Li, D. Reboredo Gil, G. H. Welsh, S. Cipiccia, B. Ersfeld, D. W. Grant, P. A. Grant, M. R. Islam, M. Shahzad, M. P. Tooley, G. Vieux, S. M. Wiggins, Z. M. Sheng, and D. A. Jaroszynski, in *Laser Acceleration of Electrons, Protons, and Ions IV*, edited by E. Esarey, C. B. Schroeder, and F. J. Grüner (International Society for Optics and Photonics, SPIE, 2017), Vol. 10240, p. 102400P.
- ⁵⁹K. Behm, A. Hussein, T. Z. Zhao, S. Dann, B. X. Hou, V. Yanovsky, J. Nees, A. Maksimchuk, W. Schumaker, A. G. Thomas, and K. Krushelnick, *Plasma Phys. Controlled Fusion* **61**, 065012 (2019).
- ⁶⁰F. Salehi, M. Le, L. Railing, M. Kolesik, and H. M. Milchberg, *Phys. Rev. X* **11**, 021055 (2021).